Article

Towards More Efficient Electric Propulsion UAV Systems Using Boundary Layer Ingestion

Jonathan Arias [1,†], Francisco Martinez [1,†], Edgar Cando [1,2,†] and Esteban Valencia [1,*,†]

1   Grupo de Investigación ATA, Departamento de Ingeniería Mecánica, Escuela Politécnica Nacional EPN, Av. Ladrón de Guevara E11-253, Quito 170525, Ecuador; jonathan.arias@epn.edu.ec (J.A.); francisco.martinez01@epn.edu.ec (F.M.); edgar.cando@epn.edu.ec (E.C.)
2   Escuela de Ingenieria Mecatronica, Universidad Internacional del Ecuador UIDE, Quito 170525, Ecuador; edcandona@uide.edu.ec
*   Correspondence: esteban.valencia@epn.edu.ec; Tel.: +593-022976300 (ext. 3726)
†   These authors contributed equally to this work.

Abstract: The implementation of distributed propulsion and boundary layer ingestion for unmanned aerial vehicles represents various challenges for the design of embedded ducts in blended wing body configurations. This work explores the conceptual design and evaluation of DP configurations with BLI. The aerodynamic integration of each configuration is evaluated following a proposed framework, including simulation analysis. Power saving coefficient and propulsive efficiency were compared against a baseline podded case. The results show the optimal propulsion configuration for the BWB UAV obtaining 3.95% of power benefit and propulsive efficiency ($\eta_p > 80\%$). Indeed, the aerodynamic integration effects for the proposed design maintain the BWB's aerodynamic efficiency, which will contribute to longer endurance and better performance.

Keywords: aerospace engineering; drones; UAV; boundary layer ingestion; ducted fans

1. Introduction

In the last decade, the aviation sector has faced rapid growth due to the expansion of civil and military applications, which impose a significant air and acoustic pollution footprint [1]. In this context, novel innovations such as blended wing body (BWB), distributed propulsion (DP), and boundary layer ingestion (BLI) have been developed to increase aircraft performance and reduce fuel consumption [2,3]. In particular, BLI technology captures a portion of the boundary layer produced along the fuselage and re-energizes it using the propulsors to dismiss the drag due to friction [4] to increase propulsive efficiency. In addition, implementing BLI coupled with embedded ducts reduces airframe weight and noise pollution [5], since embedded propulsors allow for a reduction of the wetted area and the structural weight considering the pylons' dismissal [6,7]. On the other hand, DP replaces the single propulsor with independent small propulsors, which allows for achieving high bypass ratios [8]. However, in civil aviation, the implementation of BLI with DP presents challenges related to integration and design of the airframe and embedded engines, owing to the strong regulations and large infrastructure needed for the implementation of these concepts. This makes them more complicated to adapt for current aircraft civil aviation concepts. In the case of unmanned aerial vehicles (UAV), broad design space, low costs, and lighter regulations make the aforementioned technologies suitable. Some DP technology difficulties focus on the identification of the fuel burn reduction potential [9], whereas the critical difficulty in the BLI field is the coupling effect of BLI on the aircraft fuselage. Diamantidou, Hosain, and Kyprianidis [10] compile the advances in boundary layer ingestion technology to show their advantages in fuel burn and noise reduction, reducing the environmental impact. This work shows the state of the art in the last decade, where notable designs include the hybrid wing body (HWB) and blended wing

body (BWB) concepts. These aircraft combine the airframe with propulsion interaction. In the most notable examples, the N2B and N3-X concepts have better performance for low fan pressure ratios. The use of rear-mounted engines, where propulsors are located aft of the fuselage, leads to improved system performance. The D8 concept is an example of this category, where the benefit is affected by ingested dissipation, propulsor jet velocity, and BLI installation. The propulsive fuselage concept (PFC) model absorbs the central part of the airframe boundary layer by a propulsor located at the aft part of the fuselage, since its viscous drag is one of the largest portions compared to the aircraft's viscous drag, as mentioned by the authors of Ref. [10]. According to the article, the STARC-ABL concept is one of the most well-known PFC models, which shows the importance of coupled simulations and shows where lower FPR (fan pressure ratio) is favorable. Budziszewski and Friedrichs [11] analyzed the power reduction of a BLI system vs. a pylon configuration through a parallel compressor model approach, where a propeller was located at the rear upper region of the fuselage of the aircraft where low velocity and non-uniform flow are present. Results showed a significant reduction in power consumption of the fans, leading to a 5.4% power saving coefficient. Some methodologies, such as the power balance method [12] and exergy-based assessment [13], have been developed for solving this effect and have proven their application to BLI [14]. Those frameworks are intended to start with a defined freestream velocity, and then the aircraft weight is found. In the present article, the authors propose to do it in reverse; that is, based on the aircraft weight, the BLI benefit over conventional podded propulsor configurations is determined. The present design focuses on the aerodynamic advantages of BLI over conventional podded engine configurations for the representative BWB NASA X-48B in DP arrangements.

2. Materials and Methods

2.1. Framework of Analysis

This article focuses on developing a conceptual design based on a set of configurations. The NASA X-48B UAV is selected as the reference airframe due to its BWB advantages over conventional topologies. The general framework of analysis is presented in Figure 1. First, a geometric module is used to describe the UAV airframe and propulsor allocation along the wingspan available. Then, an in-house CFD (computational fluid dynamics) case allows for finding the factor $k = V_1/U_\infty$ for the fuselage. Finally, a propulsion module analyzes the desirable cruise velocity, propulsive efficiency, and power consumption reached based on aircraft weight. In the following subsections, the aforementioned routines are described.
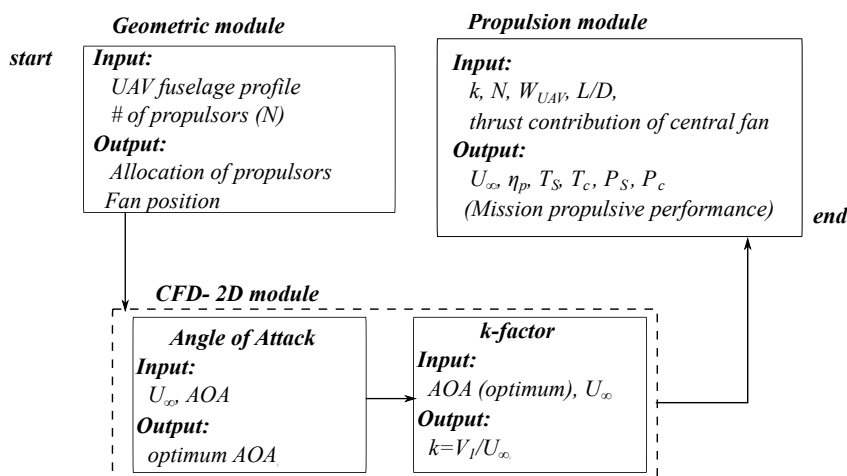

Figure 1. General methodology applied.

UAV Characteristics

Some characteristics of the aircraft under study must be improved in the present project, such as maximum take-off weight (MTOW) and propulsive efficiency, as seen in Table 1.

Table 1. Characteristics of the model.

Feature	MTOW	Propulsive Eff.
Actual	226 kg (including 3 jets and 13 gallons of fuel [15])	not given
Desired Design	<226 kg	>85%

2.2. Geometric Module

The NASA X-48B vehicle [16], which is well-known for its BWB and DP technology potential, is used as the case study. Figure 2 shows this airframe. Previous investigations [4] focused on the duct performance for BLI S-shaped embedded configurations and referred to geometrical aspects and fan distribution on the wingspan, which is employed in this research. The propulsors are intended to be equally distanced as shown on the left side of Figure 2. For stability advantages, an odd number of propulsors is preferred. Regarding Figure 2, there are two kinds of propulsors: central and distributed. The first one is located in the central chord or midspan of the UAV, and the other is uniformly located over the sides of the wingspan.
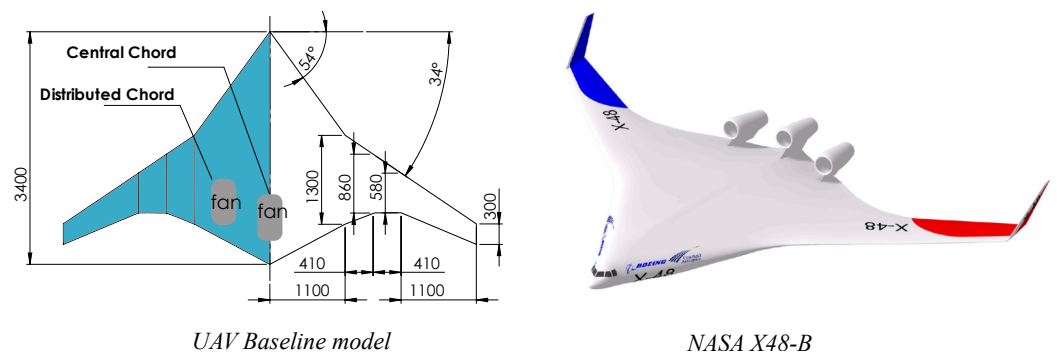

UAV Baseline model   NASA X48-B

Figure 2. UAV geometry of NASA X-48B airframe.

The fuselage profile is important in determining the UAV cruise performance. Figure 3 shows the two main configurations assessed in this paper—podded engine and BLI—with their respective control zones (upper right of this figure). In podded configurations, the freestream velocity is input directly into the ducted fan inlet and $U_\infty = V_1$, whereas in BLI, a variation is present. Rotor allocation is also presented (bottom of Figure 3), which is proposed to be located at 0.85 of the chord length. Other important aspects are the height (H) at the nacelle inlet, which is found assuming a semicircular shape at this point. This value is obtained through the continuity equation in order to achieve certain velocity V_4 for a specific V_1 mission (propulsion module calculations), and the nacelle length upstream the duct is 3.4 times the rotor diameter, as in previous designs in Ref. [4].

In this investigation, the authors established a methodological framework that shows good results in representing the phenomenon of BLI. A 2D CFD simulation is used to obtain a velocity profile at the entrance of the nozzle (BLI case), and then the standard deviation of this velocity is computed to obtain the value of V1. The authors developed a factor *k* by dividing V_1 by the freestream velocity. This factor predicts the velocity reduction effect due to the fuselage's hidden pylons, as shown in Figure 3. This *k* factor is used to quantify the duct incoming velocity in terms of the freestream value for the BLI case, forming a $k = V_1/U_\infty$ ratio, in a similar way to U_j/U_∞ in Ref. [17]. This *k* factor is allowed to vary from 0 to 1. In order to achieve the best assessment, this factor has to be as large as possible.
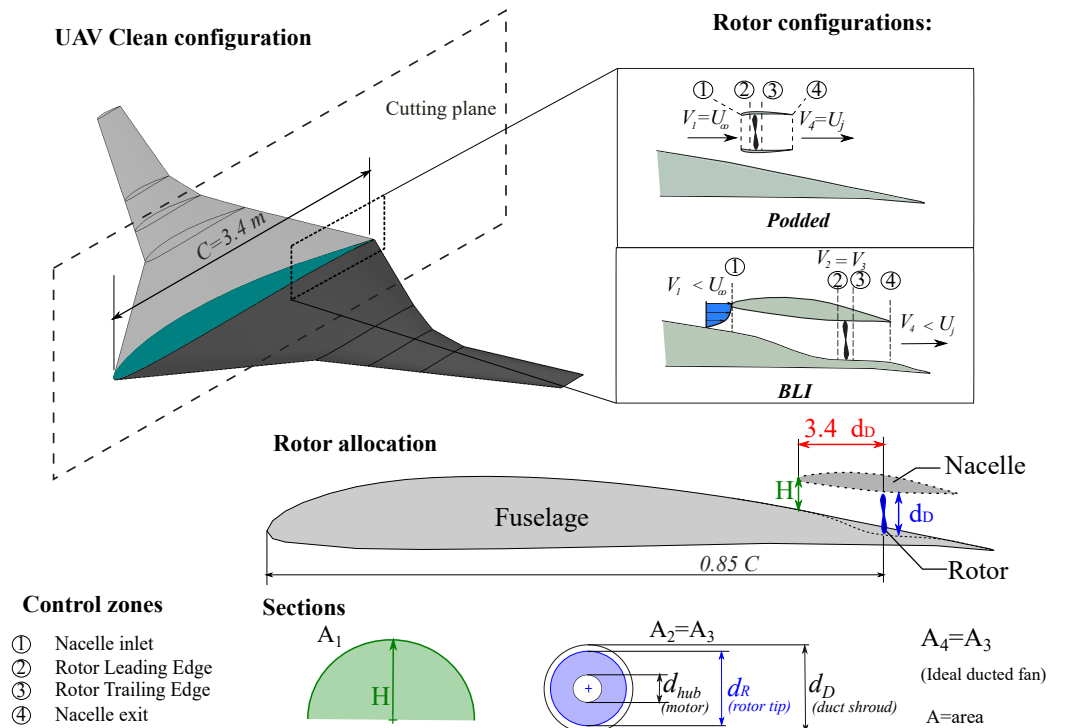
Figure 3. UAV clean configuration (**upper left**), control zones of podded vs. BLI configuration (**upper right**), and rotor allocation with control zone sections (**bottom**) of the ducted fan.

2.3. In-House CFD Case Study

A CFD analysis was performed to determine the factor k ($k = V_1/U_\infty$ is only valid for BLI, since $k = 1$ in the pylon configuration). The fuselage's optimum angle of attack (AOA) was determined at different velocities. The SD7032 airfoil was used as the fuselage in the present case study, as in Ref. [4]. For this part, the $k - \omega$ turbulence model was employed for the flow prediction capability at separated regions with low Reynolds numbers [18]. The effects of separation region are minimal due to the low Mach and Reynolds numbers used in this specific case. Hence, the methodology captures the behavior of the boundary layer.

Mesh and Boundary Conditions

The mesh was created by following the guidelines of Valencia et al. [4], who employed different grades of refinement and discovered that the best option considers a grid of 88,200 elements. The grid consists of a C topology to form the aerodynamic profile in the CFD (computational fluid dynamics) simulation. The first element length is set up with a factor of $y^+ = 1$, and the boundary conditions are inlet velocity, outlet pressure, and walls in the profile, as in Figure 4. The fluid is air at 3000 m above sea level, which is representative of Quito, Ecuador, where previous work was performed.
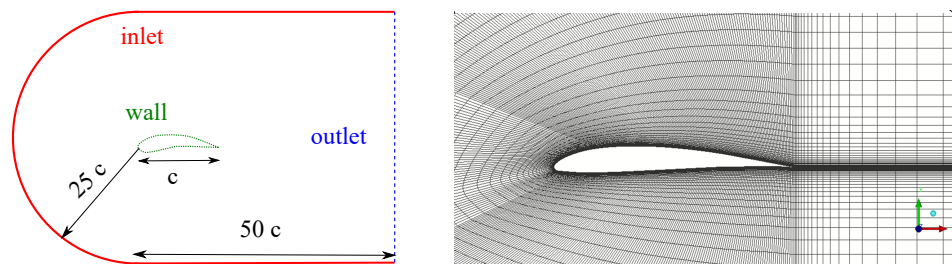
Figure 4. Mesh topology and boundary conditions used in the SD7032 fuselage CFD [4].

2.4. Propulsion Module

The next section covers the calculations implemented, and Figure 5 shows the analysis scheme. The configurations assessed here are BLI and podded engine with an odd number of fans and employ the geometry and *k* factor obtained from the previous modules. Moreover, homogeneous and non-homogeneous configurations are evaluated. Rotors are called central and distributed depending on their position relative to the wingspan. For homogeneous configurations, each fan will generate the same amount of thrust (in cruise). However, in non-homogeneous configurations, each of the fans will generate a different amount of thrust, as shown in Figure 6.

Figure 5. Propulsion module.

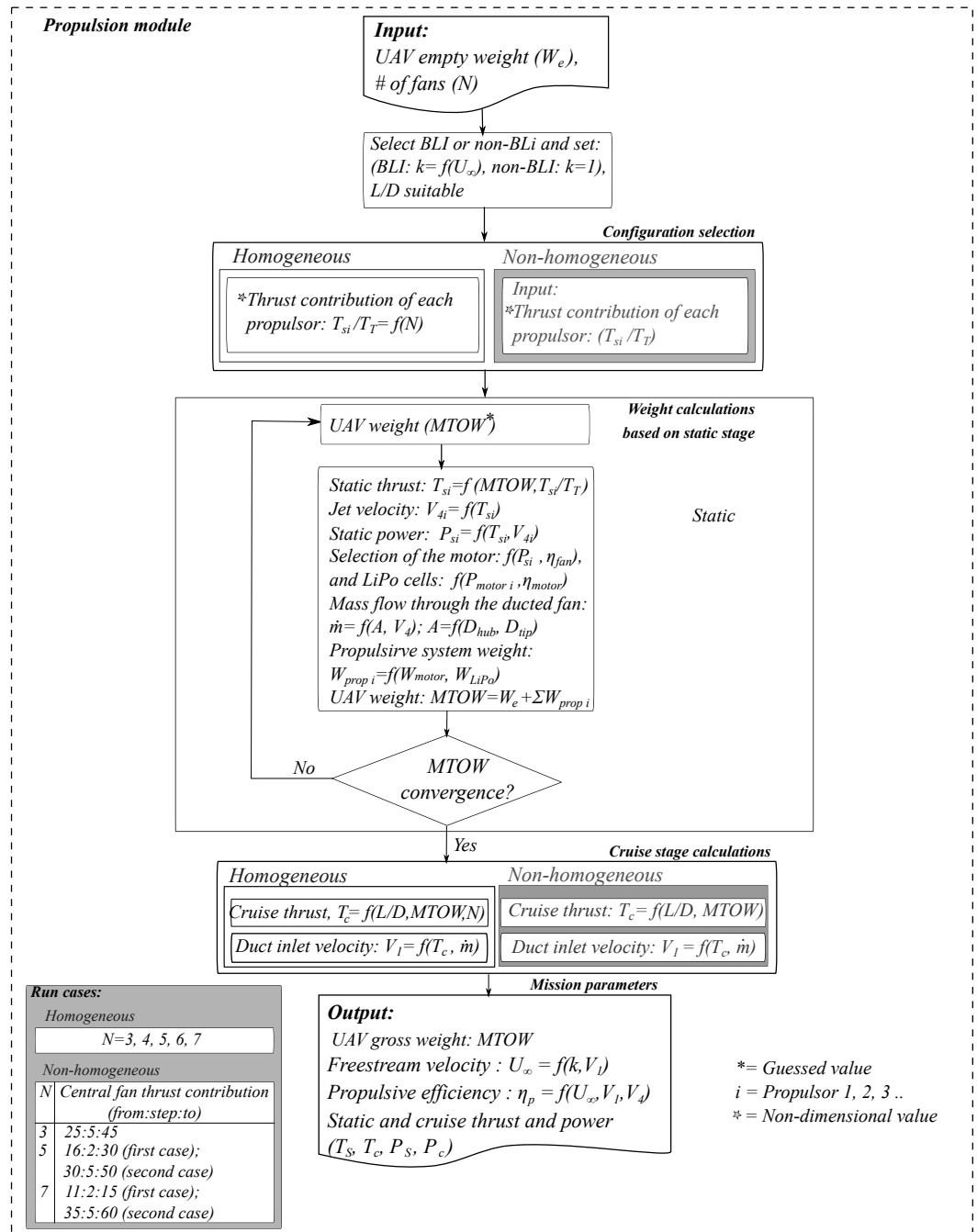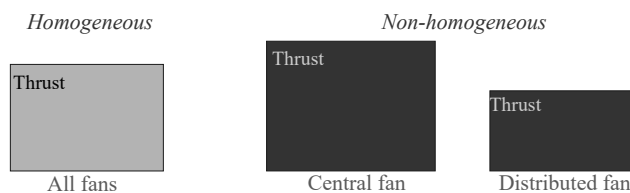*Homogeneous*　　　　　　　　*Non-homogeneous*

Figure 6. Homogeneous vs. non-homogeneous static thrust scheme.

2.4.1. Parametric Formulation for Thrust Contribution

Regarding the control zones of a classic propulsion system for both podded and BLI propulsors (see Figure 3), two stages of the flight are taken to size the rotors: static and cruise. The approach of static thrust is taken since it is the maximum force applied before moving the plane. On the other hand, the cruise stage represents the minimum force. Both stages must be satisfied. Some correlations of thrust and power for both stages are developed from Equations (1)–(6). For an ideal ducted fan ($V_3 = V_4$), which means the same area from the rotor through the nozzle [19], Equation (1) is obtained. For cruise, the four acting forces (lift, drag, weight, and thrust) are in equilibrium, as in Equation (2). Thus, the relationship of the cruise to the static thrust of Equation (3) is obtained. In the same way, for power, Equations (4) and (5) give the ratio in Equation (6).

Propulsive efficiency is well-known as $2U_\infty/(V_1 + V_4)$ [17], but it is transformed in terms of the proposed $k = V_1/U_\infty$ factor, as in Equation (7). It is worth remembering that $V_1 = U_\infty$ in the podded engine configuration and therefore $k = 1$ in that case. In the following equations, A represents the disk area (A_2 of Figure 3). Some geometric relations are employed such as $d_{hub}/d_{tip} = 0.3$ [20], which enables thermal equilibrium in the motor concerning the flow, and a tip clearance of 2% (i.e., $d_{tip}/d_D = 0.98$) [21] to diminish leakage flows in the rotor tips.

$$T_S = 2\,\Delta p\,A \tag{1}$$

$$T_c = \frac{W_T}{L/D} = \dot{m}\,(V_4 - V_1) \tag{2}$$

$$\frac{T_c}{T_S} = 1 - \frac{V_1}{V_4} \tag{3}$$

$$P_S = T_R\,V_3 = \frac{\rho\,V_3^3\,A}{2} \tag{4}$$

$$P_c = T_c\left(\frac{V_1 + V_4}{2}\right) = \dot{m}\,\frac{(V_4 - V_1)}{2} \tag{5}$$

$$\frac{P_c}{P_S} = 1 - \left(\frac{V_1}{V_4}\right)^2 \tag{6}$$

$$\eta_p = \frac{2\,U\infty}{V_1 + V_4} = \frac{2}{k + V_4/U_\infty} \tag{7}$$

2.4.2. Static Stage Model

Regarding the control zones of Figure 3, the static thrust is simplified by the Horn and Leishman ducted fan model [19], and its operation is parameterized using the Equations (8)–(12). The ideal ducted fan model is employed, which means that the duct is contributing the same thrust as the rotor ($k_{aug} = 1$). Therefore, the area is kept constant from the rotor through the nozzle ($a_w = 1$), which yields $V_4 = V_3$ as the continuity equation that must be satisfied (no compressed air). The next equations refer to each propulsor:

$$T_R = (p_3 - p_2)A = \frac{1}{2}\rho V_4^2 A \tag{8}$$

$$T_S = T_R + T_D = (1 + k_{aug})T_R = 2a_w T_R \tag{9}$$

$$k_{aug} = \frac{T_D}{T_R} \tag{10}$$

$$a_w = \frac{A_4}{A_3} = \frac{V_3}{V_4} \quad A_3 = A_2 \tag{11}$$

$$P_{fan} = V_3 T_R \tag{12}$$

2.4.3. Distributed Propulsion

Depending on their position relative to the wingspan, authors have named the rotors as central or distributed. For homogeneous configurations, each fan will generate the same amount of thrust (in cruise). However, in non-homogeneous configurations, two cases are presented:

(a) Case I: only the central fan works in cruise in order to obtain energy savings in the distributed fans.

(b) Case II: all propulsors contribute in the cruise stage.

For the homogeneous configurations, all rotors exert the same amount of thrust, as established before. Hence, the thrust contribution of each one is inversely proportional to the number of fans. In the same way, the cruise thrust is equally covered by each fan. In contrast, the two non-homogeneous cases assessed generate different amounts of thrust. In Case I, the central fan is responsible for all of the cruising force, and x is part of static thrust, whereas the distributed fans are intended to give only thrust in the static stage. As the central fan of this case is proposed to exert all the cruise force, an odd number of propulsors is preferred. In Case II, all rotors contribute to cruise thrust directly proportional to static thrust. This is represented in Figure 6. Distributed fans of the first non-homogeneous case are also planned to generate energy the way turbines do in a cruise state.

In order to determine how much thrust the central chord has to exert (in non-homogeneous configurations), the following analysis is done. In the static stage, all rotors allow the UAV to beat the friction force against the ground in order to move. The static thrust-to-UAV weight ratio for the case study is equivalent to the friction coefficient of 0.3, as mentioned by Ref. [15], which yields the total static thrust of Equation (13). A correlation between Equations (3) and (13) gives Equation (14). This represents the cruise thrust, which is equally divided by all rotors of the homogeneous cases, and only by the central fan in the non-homogeneous proposed cases.

$$T_{ST} = T_{S1} + T_{S2} + ... + T_{SN} = 0.3(MTOW) \tag{13}$$

$$\frac{T_c}{T_{ST}} = \frac{1}{0.3\,L/D} \tag{14}$$

Hence, employing the relation between Equations (3) and (14), the central rotor thrust contribution is found to be:

$$\frac{T_{S,central}}{T_{ST}} = \frac{T_c/T_{ST}}{T_c/T_S} = \frac{1}{0.3\,(L/D)\,(1 - V_1/V_4)}, \tag{15}$$

where V_1/V_4 ratio is obtained from iterative calculations. Finally, the selection of the most appropriate case either for homogeneous or non-homogeneous configurations will depend on the cruise performance results. Also, for every configuration, the velocity U_∞ is determined by applying the k factor, and a comparison between BLI and podded

configuration is achieved to compute the benefits of the power saving coefficient PSC in the operating point, as in Equation (16):

$$PSC = \frac{P_{Podded} - P_{BLI}}{P_{Podded}}.$$
(16)

2.4.4. Weight Estimation

The NASA X-48B UAV has a MTOW of 500 pounds (226.76 kg), which includes the original propulsion system (3 jets and 13 gallons of fuel capacity) [15]. Hence, operating empty weight is obtained by subtracting the jets and their fossil fuel, which results in $W_e = 181.02$ kg. A new UAV MTOW results by adding the calculated propulsive system weight of the ducted fan, as in Equations (17) and (18). Figure 7 shows propulsive system components: motor, LiPo cells selected, and 5% of them as accessories (cables, wires, connectors, etc.).
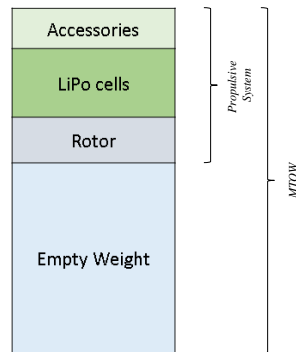

Figure 7. MTOW components.

Commercial information regarding in-runner electric motors and batteries suitable for the proposed design was used [22]. Power, weight, and number of LiPo cells of commercial products can be determined in Table 2 and then used in the calculations. LiPo cells are expected to be proportional in weight to their energy capacity, with the ratio of 0.5 kg each cell per 1800 mAh, which was estimated in terms of 30 min of flight autonomy. This flight autonomy time corresponds to the average time of the X48B scaled model tests, in accordance with Risch et al. [15].

Table 2. Benchmark data for electric motors.

Motor Class (Diameter [mm])	Power (P) [W] Min.–Max.	Weight (W) [kg]	LiPo Batteries [cells]
24	315–525	0.055	4
29	1075–1950	0.175	6
36	1950–2425	0.275	8
40	2975–4425	0.450	12
50	4425–9625	0.600	14
56	9625–14,000	1.020	19

$$W_{prop} = W_{motor} + W_{LiPo} + W_{acc}$$
(17)

$$MTOW = W_e + \Sigma W_{prop}\,; \ W_e = 181.02\,\text{kg}$$
(18)

3. Results

The authors have proposed a methodology framework that explains in detail all the parameters related to the analysis and prediction of the physical behavior of the SD7032 profile for the present investigation. Even though the form of the wing and its aerodynamic profile are different from one UAV model to another, which will affect their performance,

some parameter modifications can be done to adjust to a new model. To achieve the BLI benefits, the CFD simulation should be modified accordingly to obtain the new velocity distribution and predict the velocity reduction effect due to the fuselage's hidden pylons that define the BLI effect for a specific aerodynamic profile.

In this section, the results, analysis, and validation process are described. In the case study, the scaled NASA X-48B was selected for the ease of implementing BLI on its BWB fuselage and creating a high-efficiency airframe with low consumption. Lift-to-drag ratios of Ref. [23] are the input conditions. Other characteristics of this 8.5% scaled model are: 226 kg weight with the original jets and a static thrust-to-total weight ratio of 0.3 [15]. In order to replace the fuel-based propulsion system, the referential weight has to be reduced, and it results in 181.02 kg.

3.1. In-House CFD Case Study

In this section, the optimal angle of attack (AOA) is established by sets of FEM simulations, as seen in Figure 8. Then, the $k = V_1/U_\infty$ factor is evaluated for different freestream velocities at control zone 1, i.e., the inlet of the duct. The implemented simulation, which follows the $k - \omega SST$ model as in Ref. [4], is carefully validated with experimental C_l and C_d data as seen in the previous section. This turbulence model allows for the prediction of the flow behavior at separated flow regions or stagnation points where high adverse pressure gradients are present [18]. To select the most appropriate AOA, the minimum c_d criterion is applied to a 2nd order polynomial fitting curve, as in Ref. [4], and the results achieve the optimal AOA, which is AOA = 0.56 deg. Regarding the final part of this CFD-2D, the $k = V_1/U_\infty$ factor determination for each velocity is assessed for different U_∞ velocities. The average $\bar{V}_1$ represents the mean velocity at the control zone 1 (ducted fan inlet; see Figure 3). $\bar{V}_1$ is estimated in terms of the V_1/U ratio, until it reaches the height H necessary from the fuselage to the duct lips (see Figure 3). The H height of the duct inlet is found in the function of the area ratio $A_1/A_4 = V_1/V_4$, i.e., the non-compressible flow continuity equation, as detailed in the methodology. Now, the k factor is the ratio of this mean velocity to the maximum freestream velocity and must be less than 1 ($k < 1$) for BLI, since $k = 1$ for pylon configurations. While the velocity profile demonstrates the boundary layer separation, the contour of pressure shows the expected trend with a higher pressure zone starting at the tip.
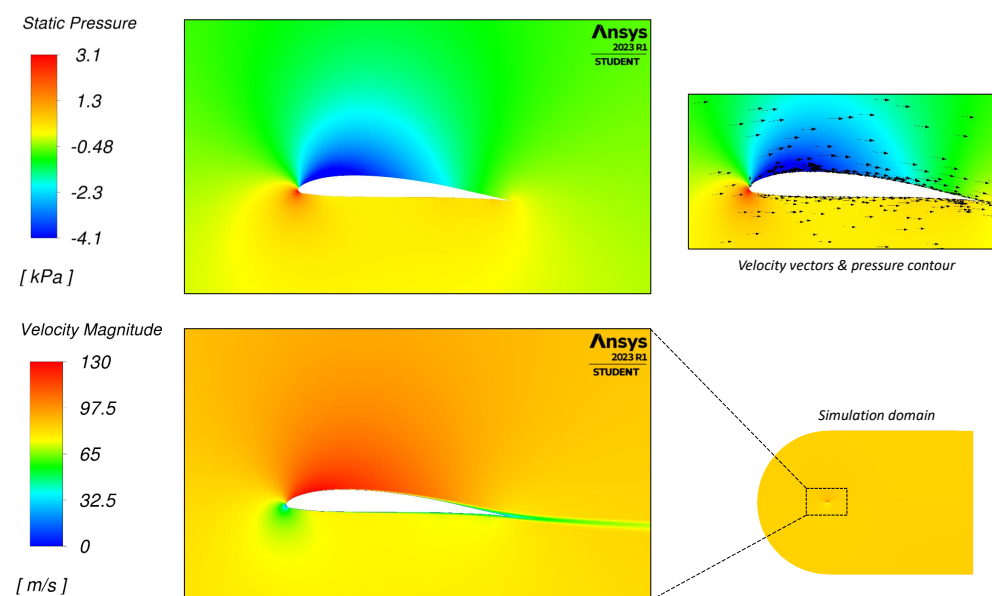

Figure 8. Typical contours of velocity and pressure for the BLI.

3.2. Propulsion Module

Calculations result in ratios of $L/D = 17.024$ for BLI and $L/D = 16.267$ for pylons [23], despite the number of propulsors and their size, which simplifies the model. Total power and total thrust refer to the sum of the number of propulsors, and the efficiencies employed for the fan and motor are $\eta_{fan} = 85\%$ and $\eta_{motor} = 90\%$, respectively [20]. First, the static stage is obtained for each configuration (homogeneous and non-homogeneous) of BLI and podded rotors. Then, the cruise stage is evaluated in order to satisfy the equilibrium of forces based on the L/D of reference. Static stage results are independent of the cruise stage; however, the latter depends on the static stage. The diameter of the central and distributed chord are estimated as a function of each fan thrust contribution, as well as the other columns of this table. In the case of non-homogeneous configurations, the central fan has x thrust contribution, and the rest of the fans have the same value, in that the total thrust contribution is equal to 100%. Total static thrust and power are also estimated, as well as aircraft weight, obtained by Equation (18). For the cruise stage, the k factor for BLI given by CFD simulations, and the $k = 1$ for podded configurations. Figure 9 shows a frontal view draft of different configurations:
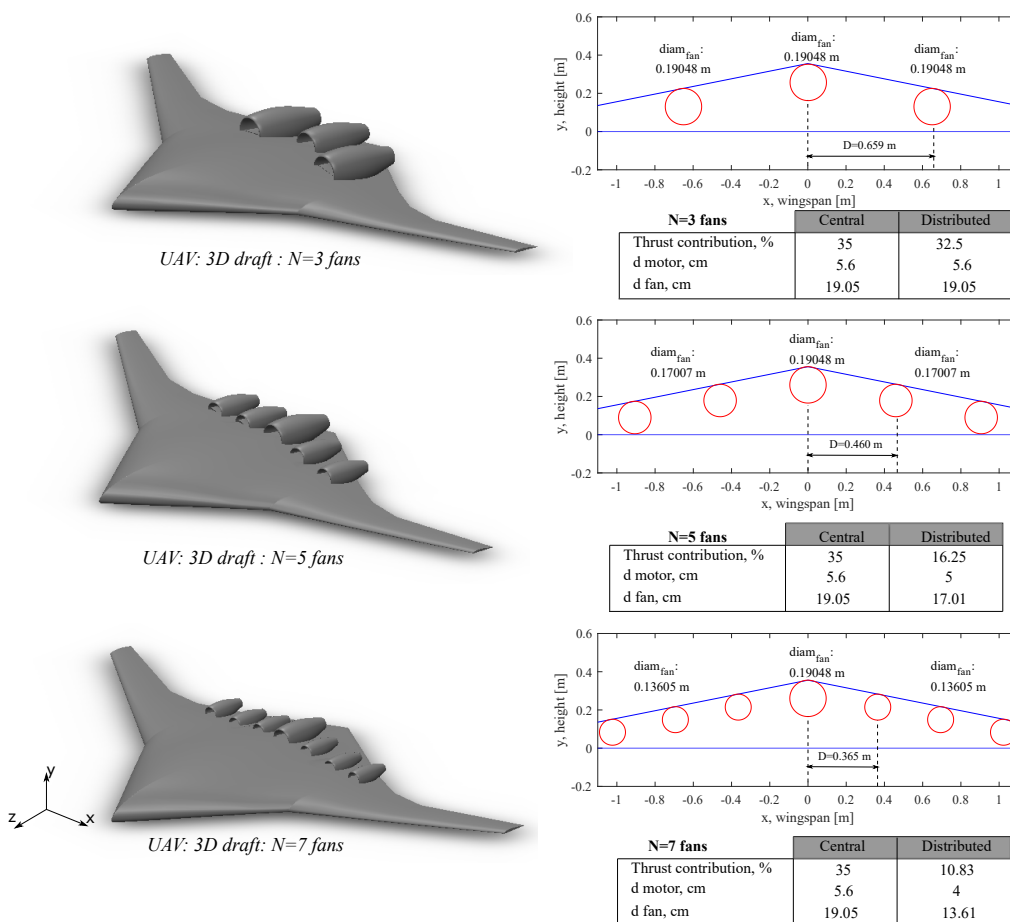

UAV: 3D draft : N=3 fans

N=3 fans	Central	Distributed
Thrust contribution, %	35	32.5
d motor, cm	5.6	5.6
d fan, cm	19.05	19.05

UAV: 3D draft : N=5 fans

N=5 fans	Central	Distributed
Thrust contribution, %	35	16.25
d motor, cm	5.6	5
d fan, cm	19.05	17.01

UAV: 3D draft: N=7 fans

N=7 fans	Central	Distributed
Thrust contribution, %	35	10.83
d motor, cm	5.6	4
d fan, cm	19.05	13.61

Figure 9. Aircraft schemes: 3D draft (**left**) and frontal view (**right**) of different configurations (particular case of thrust contribution = 35% for non-homogeneous configuration).

3.2.1. Homogeneous Configuration

Table 3 shows the static stage of homogeneous configurations for 3 to 7 propulsors. Static results were the same for the BLI and podded cases, which is due to the design being intended to generate the same thrust regardless of the BLI or non-BLI configuration. Differences can be seen in the cruise stage. For each number of fans (*N*), the motor size, thrust power, and weight are presented. Weight includes the base empty aircraft plus the fan weight, which involves the propulsive system (i.e., motor + LiPo batteries + accessories),

as in Equations (17) and (18). Final MTOW is, on average, 196.38 kg, and this implies a reduction of 12.67% with respect to the initial weight of 226.75 kg. Static results were the same for the BLI and podded cases because they refer to the static stage of the aircraft, which was taken assuming the same propulsive system weight. Differences are presented at the cruise stage, where the *k* factor is different at the entrance to the ducts, as seen in the following section.

Table 3. Static performance for BLI and podded homogeneous configurations.

Number of Propulsors (N)	Motor Diameter, cm	Total Thrust, N (T_{ST})	Total Power, kW (P_{ST})	Weight, kg UAV ($MTOW$)
3	5.6	581.06	26.28	197.70
4	5	573.91	25.02	195.27
5	5	573.57	22.36	195.15
6	5	575.40	20.51	195.77
7	5	578.20	20.37	198.02

Table 4 refers to cruise performance for homogeneous configuration. Here, the total cruise thrust and power are presented, obtaining a benefit power around 4%, which is similar to that of Refs. [12,24].

Table 4. Propulsive performance (cruise) for BLI and podded homogeneous configurations.

Number of Propulsors (N)	Total Thrust (T_{cT}), N		Total Power (P_{cT}), kW		η_p	
	BLI	Podded	BLI	Podded	BLI	Podded
3	113.772	119.079	9.284	9.668	0.938	0.886
4	112.371	117.612	8.840	9.205	0.938	0.886
5	112.305	117.544	7.899	8.226	0.938	0.886
6	112.663	117.918	7.246	7.545	0.938	0.886
7	111.748	117.063	7.112	7.412	0.938	0.885

Total cruise thrust and power contribution show a decreasing trend with the increase in the number of thrusters, and the MTOW increases (see Table 3) while the total thrust remains almost the same (Table 4). Furthermore, propulsive efficiency was almost the same for each *N*, since *L/D* ratios were the same [23].

3.2.2. Non-Homogeneous Configurations

Different thrust contributions of the central fan with respect to total static thrust were assessed to evaluate the best-case scenario considering the number of fans (*N*). For visual purposes, Figure 10 shows the scheme of the thrust contribution of the fans for 3–7 propulsors (*N* = 3, 5, 7) in the non-homogeneous configuration of the particular case of 35% of thrust contribution (central fan). This percentage was selected to illustrate differences between the configurations. In this Figure 10, the blue column represents the central fan thrust percentage contribution, with the same value of 35% for all *N*, and the red column shows different contributions for the distributed fans, depending on the total number of fans.

As mentioned before, in non-homogeneous configurations, two cases were assessed:

(a) Case I: Poor propulsive efficiency is achieved considering only the central fan works in cruise in order to obtain energy savings in the distributed fans. However, the energy saved for the distributed fans could be used to recharge the LiPo cells, working the fans like turbines. The estimation of the energy saved is proportional to the energy consumed by the distributed fans in the static stage, but a complete analysis could be done in future work.

(b) Case II: in order to optimize the η_p efficiency, all propulsors contribute in the cruise stage, but no energy can be saved and no LiPo cells recharged.
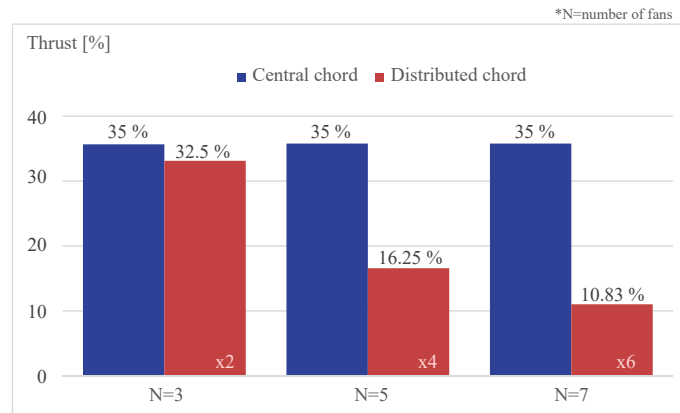

Figure 10. Percentage thrust contribution for the case: 35% central thrust in non-homogeneous configurations.

- Static Performance

Table 5 shows results for the static stage of both cases. The difference between the first and second case is the thrust contribution. In the first case (only the central chord works in cruise), the central fan has to be very big compared to the others; therefore, high thrust contribution is needed, and high power consumption was computed. For the second case (all rotors work in cruise), thrust contribution is similar to that of the homogeneous configurations. Independently of the case or thrust contribution, a small difference in total cruise thrust and total power was noted, since all of them were evaluated with the same lift-to-drag ratio L/D, as in homogeneous configurations. Other authors claim to use configurations in which the size of the rotors of the central and distributed chords do not differ much, as in the second case, avoiding affecting the frontal area of the aircraft and the L/D assumption.

Table 5. Static performance for BLI and podded non-homogeneous configurations.

Number of Propulsors (N)	Central Fan Thrust Contribution, %	Thrust, N Total (T_{ST})	Central	Distrib.	Total (P_{ST})	Power, kW Central	Distrib.	UAV Weight (*MTOW*), kg
3	25	563.462	143.477	209.993	26.035	6.256	9.890	191.71
	35	566.405	198.241	184.075	25.319	9.369	7.975	192.71
	45	568.697	261.623	153.537	27.603	13.753	6.925	193.50
5	16	576.811	92.352	121.115	22.786	3.379	4.852	196.25
	22	573.571	126.435	112.054	22.361	5.175	4.318	195.15
	30	576.811	173.021	98.173	22.030	7.397	3.541	195.42
7	11	576.142	63.059	85.514	20.579	2.278	3.050	196.03
	13	577.068	74.626	83.740	20.718	2.933	2.964	196.34
	15	576.954	86.401	81.759	23.280	3.098	3.364	196.30

UAV weight was also assessed in order to find differences, and results show that $N = 7$ is the heaviest case; despite the rotors being smaller, there are more of them. On average, 3 fan configurations give 192.75 kg of *MTOW*, which represents 15.0% of the benefit with respect to the initial UAV weight (226 kg, according to Ref. [15]). For 5 and 7 fans, the results are average weights of 195.69 kg and 196.22 kg, with a benefit of 13.7% and 13.5%, respectively.

- Cruise performance

Whereas in the static stage, BLI and podded configurations have almost the same values of thrust, power, etc., because the same rotors are used, for the propulsive performance, more notable differences are observed. (Note that, as central fan weight increases

with thrust contribution, the distributed fan weight decreases because of the lower thrust needed in that chord.) The first case (only one central fan in cruise) is presented in Table 6, and the second case (all fans in cruise with different thrust contributions) is presented in Table 7.

Table 6. Propulsive performance (cruise-only central fan) for BLI and podded non-homogeneous configurations.

Number of Propulsors, (N)	Central Fan Thrust Contribution, %	Total Thrust (T_{cT}), N		Total Power (P_{cT}), kW		η_p, -	
		BLI	Podded	BLI	Podded	BLI	Podded
3	25	109.944	115.242	5.914	6.013	0.399	0.329
	35	110.868	116.211	7.449	7.667	0.656	0.598
	45	111.376	116.744	9.217	9.536	0.768	0.713
5	35	110.868	116.211	7.449	7.667	0.656	0.598
	45	111.376	116.744	9.217	9.536	0.768	0.713
7	35	110.868	116.211	7.449	7.667	0.656	0.598
	45	111.376	116.744	9.217	9.536	0.768	0.713
	55	112.211	117.618	10.811	11.217	0.831	0.777

Table 7. Propulsive performance (all cruise fans) for BLI and podded non-homogeneous configurations.

Number of Propulsors, (N)	Central Fan Thrust Contribution, %	Thrust BLI (T_{cT}), N		Thrust Podded (T_{cT}), N		Total Power (P_{cT}), kW		η_p, -	
		Central	Distrib	Central	Distrib	BLI	Podded	BLI	Podded
3	25	19.722	46.737	21.127	48.674	9.595	9.990	0.975	0.921
	35	43.643	34.778	45.447	36.516	9.224	9.605	0.926	0.874
	45	66.780	23.343	68.993	24.883	10.095	10.507	0.899	0.848
5	16	9.232	25.927	10.176	27.008	8.061	8.394	0.997	0.942
	22	29.463	20.763	30.564	21.800	7.938	8.266	0.914	0.863
	30	48.845	15.903	50.255	16.862	7.858	8.178	0.880	0.830
7	11	15.459	16.225	16.000	17.012	6.912	7.198	0.906	0.855
	13	22.744	15.041	23.333	15.821	6.988	7.274	0.863	0.815
	15	4.558	18.068	5.488	18.792	8.253	8.592	1.022	0.965

As seen in Table 6, which represents case *a* of the analysis, high values of central fan thrust contribution are observed. This fan has to be greater than that of the second case to generate the total cruise thrust necessary (T_{cT}) for the mission, and propulsive efficiency is lower in the first case. The values of both cases can be compared in terms of total power and propulsive efficiency. Comparing the $N = 3$ cases, Table 6 shows minor total power, which is a benefit for energy consumption, but poor propulsive efficiency because of the nozzle velocity achieved in those thrust requirements. However, the other configurations of $N = 5$ and $N = 7$ fans in Case I have better efficiency, comparable with those in Case II.

Additionally, a table including the weight of every component of the propulsive system is attached to the *Appendix* section, where 35% of thrust contribution is presented. The following table shows similar results for case *b*, where all rotors work in cruise. Different percentages were evaluated for the value of homogeneous configurations, since all rotors work in cruise, as seen in Table 7.

Comparing cruise performance of both cases of non-homogeneous configurations (Tables 6 and 7), the total power has smaller values in the first case involving 3 propulsors, and in some of the $N = 5$ cases.

Values of η_p are preferred in the central fan, in order to address the most representative rotor. Higher values of propulsive efficiency were obtained in the second case (all fans in cruise), leading to the possibility of flying at higher velocities (U_∞). All of this shows the advantage of working with all fans on cruise. The power benefit was assessed through a graphic, which shows a representative savings only in the second case where, despite the number of fans N, this savings remained almost constant.

3.3. Validation

In this section, the authors explain the validation process of the propulsion model and the comparison of the in-house CFD case against experimental data, as shown Table 8. The ideal ducted fan model [19] was compared to commercial products [25], and Equations (8)–(12) employed provide the following results.

Table 8. Validation of the propulsion module vs. benchmark data quantities [25].

Product	Parameter	Product Specifications	Propulsion Module Calculations	Error %
Schubeler DS-215-DIA	Thrust (T_S), kg	24	24.404	1.68
HST 195 mm Carbon	Power ($\dot{W}_S$), kW	13	12.28	5.54
DEDF Ducted Fan + Motor	Duct diameter (d_D), cm	19	19.5	2.63
DSM10066-290	Disk area (A), cm^2	250	249.04	0.38
	Velocity (V_3), m/s	98	102.76	4.86
Ducted Fan EDF	Thrust (T_S), kg	5	5.03	0.60
JETFAN-100 Pro Ejets	Power ($\dot{W}_S$), kW	2	1.79	10.50
+ HET 700-98-935 motor	Duct diameter (d_D), cm	10	12.25	22.5
Schubeler-ds-82-hst-	Thrust (T_S), kg	12	12.71	5.92
v2016-120mm carbon	Power ($\dot{W}_S$), kW	7	8.47	21.00
-edf-ducted-fan-dsm	Duct diameter (d_D), cm	12	11.463	4.75
-6043-650kvmotor	Disk area (A), cm^2	82	73.89	9.89
	Velocity (V_3), m/s	110	136.13	23.75

The previous results correspond to the parametric model with a 0.3 hub-to-tip ratio, but for the last results (Schubeler-ds-82), this ratio was assumed to be 0.5 since it was not given [25]. FEM simulation was assessed considering the $k - \omega SST$ turbulence model of Ansys Fluent. CFD worked at an AOA = 0, with a chord of 1 m and a Reynolds number of 2×10^5 [4] for the SD7032 fuselage profile. As described in the methodology, the mesh was assessed by the guidelines in Ref. [4] and by $y^+ = 1$, which yields 5.32×10^{-5} m as the first cell length. Results show good agreement compared to the lift and drag coefficient of the experimental data [26], as seen in Figure 11.
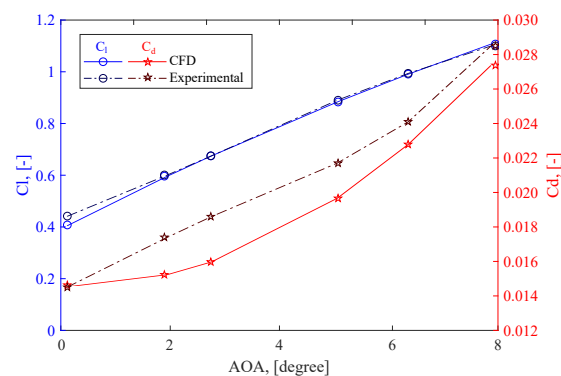

Figure 11. Lift (left) and drag (right) coefficients of the SD7032 profile for validation: experimental [26] vs. CFD of the present article.

4. Discussion

The following analysis demonstrates phenomena in the cruise stage where propulsive performance is evaluated. Results were plotted in the same way as in Ref. [24], with power benefit along the *y* axis and propulsive efficiency along the *x* axis for non-homogeneous configurations. On the left side of Figure 12, which represents Case I, an ordered behavior was observed. However, for the second case (right side of this figure), a scatter plot was achieved. The PSC (power saving coefficient) is the complement of power benefit. Comparing the trends in Ref. [24], where a decreasing curve was observed, Case I agrees very well, which validates the present methodology. In general, non-homogeneous configurations of the second case are characterized by its scattered trend, and the first case has more ordered points. This is because, in the first case, only one fan is used at cruise and all variables depend on themselves: η_p, U_∞, and power consumption. However, in the second case, all rotors are interacting in cruise, and this yields different V_1/V_4 ratios for each fan.
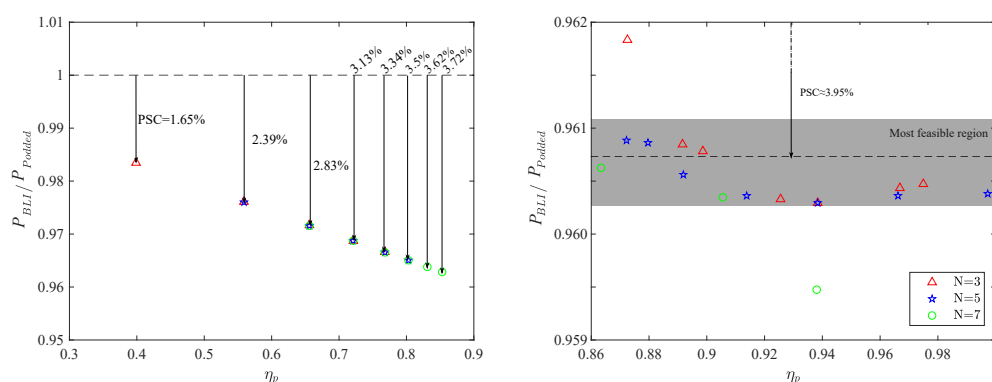

Figure 12. Cruise power benefit vs. propulsive effect for non-homogeneous configurations, Case I (**left**) and Case II (**right**).

As seen in Figure 12, it is better to work with Case II in terms of non-homogeneous configurations (right side of this figure), due to the better propulsive efficiency and power benefit. The most feasible area is also presented and belongs to the zone of higher point density and higher values, with power benefit around 3.95% (see Figure 12). The $N = 5$ propulsors case is all inside this zone, whereas $N = 3$ and $N = 7$ each have one point outside this area. The best configuration is said to be the one that has less power consumption and higher efficiency η_p. This configuration yields $N = 5$ propulsors for better propulsive efficiency ($\eta_p = 0.997$), which corresponds to the thrust contribution of 16%. It is better to work with a value close to that of the homogeneous configuration (20%), which will give fewer differences in rotor sizes. Thus, the mechanical maintenance will be achieved without great effort.

As a final note, depending on the UAV used in the case study, two main aspects affect the calculations. First, the L/D ratio has to refer to the airframe of study. For the UAV X-48B, this was estimated by Ref. [23], which says that, for BWB, $L/D = 17.024$ for BLI and $L/D = 16.267$ for pylons. They both remained constant for every configuration assessed in this article. However, if the aircraft under study is not a BWB, these coefficients would change, and a referential value would be needed. In addition, this factor depends on the number of propulsors, their size, and allocation along the wingspan. Second, the *k* factor determination strongly depends on the position along the wingspan, chord of the ducted fan inlet, and the size of it. Here, this *k* remained the same independent of freestream velocity. Different results will be obtained for different heights of duct inlets and chord positions, even if the ducted fan is the same. Finally, the airframe geometry and weight used need to correspond to scaled airplanes (the present case of study X-48B is an 8.5% scale model [19] of the full-scale BWB) in order to not exceed the power motors can handle (see Table 2). A referential value is 200 kg, as in this article, but the present authors recommend

using lighter-weight UAVs if possible. The CFD analysis is a useful tool to understand the phenomena of the configurations related to BLI cases. The authors recommend further study of this topic by assuming ranges of distortion of the pressure field and by using and comparing different methods to evaluate integration effects of aerodynamic surfaces. An extensive analysis should be performed to reach proper noise reduction. This could be developed by obtaining the pressure fields under various conditions to capture the effect of vibration of the components, especially fan blades. Indeed, the design of the inlet and S-ducted fan will be critical for appropriate noise reduction. The length and height of the S-duct upstream from the rotors, which is the main cause of distortion in the flow, means that blades will produce fewer vibrations if the flow is more uniform.

5. Conclusions

This paper presented a formulation for the sizing of ducted fans for BLI configurations with a distributed propulsion system, based on the X-48B of NASA. Some cases were assessed in homogeneous and non-homogeneous configurations. For the homogeneous ones, 3 to 7 fan variations were assessed, reaching a power-saving benefit around 3.95% and propulsive efficiency around 96%. In contrast, the non-homogeneous configurations considered odd numbers of propulsors in order to maintain the structural equilibrium of the UAV. Some differences, such as an increase in PSC, propulsive efficiency, and freestream velocity, were documented. Comparing the homogeneous configurations and the first non-homogeneous case, the graphics were well-ordered in a decreasing trend of power benefit (compliments of PSC) vs. propulsive efficiency, which showed a validation of this methodology. Working with $N = 5$ propulsors was found to be the best option in terms of propulsive efficiency, since the power benefit remained practically the same for the Case II configurations. Finally, weight reduction was accomplished by a factor of 13%. The second case of heterogeneous configurations (all fans contribute in cruise) resulted in the best option for higher PSC, η_p, and U_∞, and less power consumption than that of the homogeneous configuration.

Author Contributions: Conceptualization, E.V.; methodology, J.A.; software, J.A.; validation, J.A. and F.M.; formal analysis, E.C.; investigation, J.A.; resources, E.V.; writing, J.A. and F.M.; supervision, E.V. All authors have read and agreed to the published version of the manuscript.

Data Availability Statement: Not applicable.

Conflicts of Interest: The authors declare no conflicts of interest.

References

1. Bruner, S.; Baber, S.; Harris, C.; Caldwell, N.; Keding, P.; Rahrig, K.; Pho, L.; Wlezian, R. *NASA N+ 3 Subsonic Fixed Wing Silent Efficient Low-Emissions Commercial Transport (SELECT) Vehicle Study. Revision A*; NASA/CR: Cleveland, OH, USA, 2010; pp 1–187.
2. Abbas, A.; De Vicente, J.; Valero, E. Aerodynamic technologies to improve aircraft performance. *Aerosp. Sci. Technol.* **2013**, *28*, 100–132. [CrossRef]
3. NASA Technical Reports Server. *Review of Propulsion Technologies for N+ 3 Subsonic Vehicle Concepts*; AIAA: Cleveland, OH, USA, 2011.
4. Valencia, E.A.; Ayala, M.; Hidalgo, V.; Simbaña, S.; Alulema, V.H.; Rodriguez, D.; Cando, E. Aeropropulsive Evaluation of Boundary Layer Ingestion for Medium Electric-Powered UAVs. In Proceedings of the AIAA Propulsion and Energy 2020 Forum, Virtual Event, 24–28 August 2020; Volume 1, pp. 1–16.
5. Plas, A.; Crichton, D.; Sargeant, M.; Hynes, T.; Greitzer, E.; Hall, C. Madani, V. *Performance of a bOundary Layer Ingesting (BLI) Propulsion System*; Session: AD-3: The Silent Aircraft Initiative; AIAA: Orlando, FL, USA, 2007.
6. NASA Technical Reports Server. *Turboelectric Distributed Propulsion Engine Cycle Analysis for Hybrid-Wing-Body Aircraft*; AIAA: Orlando, FL, USA, 2009.

7. Liu, C. Turboelectric Distributed Propulsion System Modelling. Ph.D. Dissertation, Cranfield University, Bedford, UK, 2013.
8. Goldberg, C.; Nalianda, D.; Pilidis, P.; MacManus, D.; Felder, J. Installed performance assessment of a boundary layer ingesting distributed propulsion system at design point. *J. Propuls. Power* **2016**, *52*, 1–22.
9. Habermann, A. *Effects of Distributed Propulsion on Wing Mass in Aircraft Conceptual Design*; AIAA: Orlando, FL, USA, 2020; Volume 2625.
10. Diamantidou, D.E.; Hosain, M.L.; Kyprianidis, K.G. Recent Advances in Boundary Layer Ingestion Technology of Evolving Powertrain Systems. *Sustainability* **2022**, *14*, 1731. [CrossRef]
11. Budziszewski, N.; Friedrichs, J. Modelling of a Boundary Layer Ingesting propulsor. *Energies* **2018**, *11*, 708. [CrossRef]
12. Drela, M. Power Balance in Aerodynamic Flows. *AIAA J.* **2012**, *47*, 1761–1771. [CrossRef]
13. Arntz, A.; Atinault, O.; Destarac, D.; Merlen, A. *Exergy-Based Aircraft Aeropropulsive Performance Assessment: CFD Application to Boundary Layer Ingestion*; AIAA: Orlando, FL, USA, 2014; Volume 2573.
14. Hall, D.K.; Huang, A.C.; Uranga, A.; Greitzer, E.M.; Drela, M.; Sato, S. Boundary Layer Ingestion Propulsion Benefit for Transport Aircraft. *J. Propuls. Power* **2017**, *33*, 1118–1129. [CrossRef]
15. Risch, T.; Cosentino, G.; Regan, C.; Kisska, M.; Princen, N. X-48B Flight-Test Progress Overview. In Proceedings of the 47th AIAA Aerospace Sciences Meeting Including the New Horizons Forum and Aerospace Exposition, AIAA, Orlando, FL, USA, 5–8 January 2009.
16. Griffin, B.; Brown, N.; Yoo, S. Intelligent Control for Drag Reduction on the X-48B Vehicle. In Proceedings of the AIAA Guidance, Navigation, and Control Conference, Portland, OR, USA, 8–11 August 2011.
17. Bevilaqua, P.; Yam, C. Propulsion Efficiency of Wake Ingestion. *J. Propuls. Power* **2020**, *36*, 517–526. [CrossRef]
18. Menter, F.R. Two-equation eddy-viscosity turbulence models for engineering applications. *AIAAJ* **1994**, *32*, 1598–1609. [CrossRef]
19. Montgomery, L. Aerodynamic Experiments on a Ducted Fan in Hover and Edgewise Flight. Master's Thesis, The Pennsylvania State University, State College, PA, USA, 2009.
20. Jin, Y.; Qian, Y.; Zhang, Y.; Zhuge, W. Modeling of Ducted-Fan and Motor in an Electric Aircraft and a Preliminary Integrated Design. *J. Aerosp.* **2018**, *11*, 115–126. [CrossRef]
21. Akturk, A.; Camci, C. Tip Clearance Investigation of a Ducted Fan Used in VTOL UAVS: Part 1—Baseline Experiments and Computational Validation. *J. Turbomach.* **2011**, *7*, 331–344.
22. Brushless Motors. Available online: https://www.turbines-rc.com/en/25-brushless-motors (accessed on 14 April 2023).
23. Rodriguez, D.L. Multidisciplinary optimization method for designing boundary-layer-ingesting inlets. *J. Aircr.* **2009**, *46*, 883–894. [CrossRef]
24. Uranga, A.; Drela, M.; Hall, D.K.; Greitzer, E.M. Analysis of the Aerodynamic Benefit from Boundary Layer Ingestion for Transport Aircraft. *AIAA J.* **2008**, *56*, 4271–4281. [CrossRef]
25. EDF & Turbines. Available online: https://www.turbines-rc.com/en/132-schubeler (accessed on 16 April 2023).
26. Selig, M.S.; Guglielmo, J.J.; Broeren, A.P.; Giguere, P. *Summary of Low-Speed Airfoil Data*; SoarTech Publications: Virginia Beach, VA, USA, 1995; Volume 1.